Supplement of Atmos. Meas. Tech., 15, 1811–1827, 2022
https://doi.org/10.5194/amt-15-1811-2022-supplement

Atmospheric Measurement Techniques
Open Access
EGU

Supplement of

Fragmentation inside proton-transfer-reaction-based mass spectrometers limits the detection of ROOR and ROOH peroxides

Haiyan Li et al.

Correspondence to: Haiyan Li (lihaiyan2021@hit.edu.cn), Mikael Ehn (mikael.ehn@helsinki.fi), and Theo Kurtén (theo.kurten@helsinki.fi)

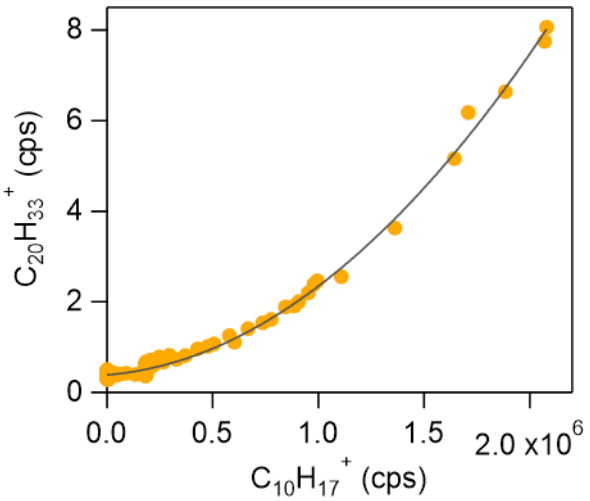

Figure S1. Correlation plot of $C_{10}H_{17}^+$ and the secondary ion cluster $C_{20}H_{33}^+$.

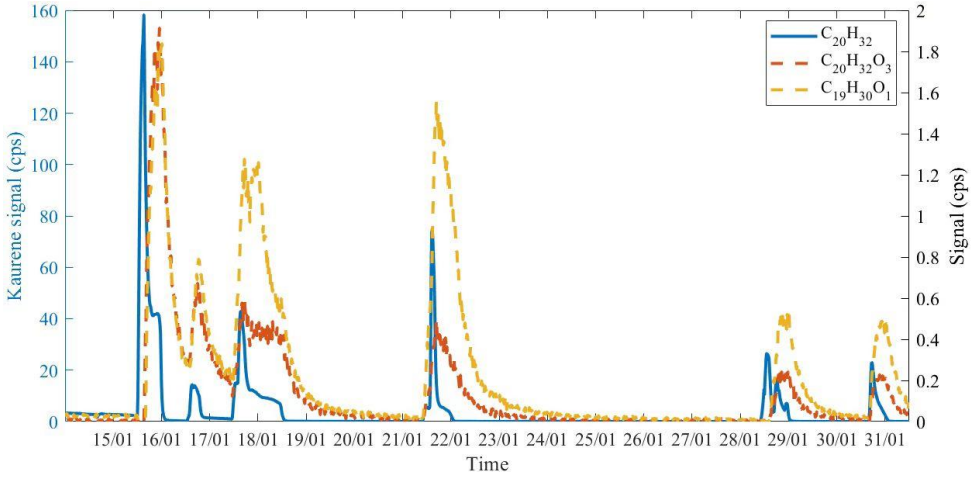

Figure S2. Time series of kaurene ($C_{20}H_{32}$) and its oxidation products $C_{19}H_{30}O$ and $C_{20}H_{32}O_3$ during the kaurene oxidation experiment.

S1 MESMER simulations.

Once the PES of each model ROOR and ROOH system was obtained, the time-dependent species distribution profile was estimated with MESMER (Master Equation Solver for Multi-Energy Well Reactions) version 6.0 (Glowacki et al., 2012). Together with zero-point corrected energies, vibrational frequencies and rotational constants for each stationary point were used as input. Since the investigated reactions happen in low pressures, and are preceded by an exothermic protonation step (Rp), kinetic and collisional relaxation time scales may be of similar magnitude. In such cases, Rice-Ramsperger-Kassel-Marcus (RRKM) theory offers a more appropriate treatment, and was accordingly used to model all isomerization steps in the master equation. The imaginary frequency of each transition state (mode associated with the reaction motion), was provided for calculation of the

Eckart tunnelling factor (Eckart, 1930). Irreversible dissociation steps were assumed to be barrierless, and were treated with the reverse Inverse Laplace Transformation (ILT) method. The Arrhenius pre-exponential factor was estimated according to a parameterized procedure for obtaining ion-dipole collision rates reported by (Su and Chesnavich, 1982), giving values in the range of 1~4 x 10^{-9} cm^3 $molecule^{-1}$ s^{-1}. A modified Arrhenius parameter (n^{∞}) value of 0.01 was used. The protonation step could not be modelled explicitly, because the treatment of bimolecular exchange reactions in MESMER requires a transition state, which was not found. Thus, the initial charged species (RH^+) was modelled as having emerged from a barrierless dissociation reaction, $A(E_{ex}) \rightarrow RH^+ + H_2O$, where E_{ex} is the excess energy in reactant A, which was assumed to be equal to the zero-point corrected energy of reaction R1p (ΔE_{zp}). This could be done by using the Prior method for the initial distribution of states, where the E_{ex} is shared between the dissociation products according to a probability distribution. The probability that RH^+ emerges from the reaction with energy E is given as described in MESMER's manual:

$$p_{ROORH^+}(E, E_{ex}) = \frac{\rho_{ROORH^+}(E)\ .\ [\rho_t * \rho_{H_2O}](E_{ex} - E)}{[\rho_{ROORH^+} * \rho_t * \rho_{H_2O}](E_{ex})}$$

Where $\rho_{ROORH^+}(E)$ and ρ_{H_2O} are the rovibrational density of states of RH^+ and H_2O respectively, and ρ_t is the relative translational density of states of RH^+ and H_2O. The expression $[x * y](E)$ is a convolution:

$$[x * y](E) = \int_0^E x(E - \tau)y(\tau)d\tau$$

The exponential down model was employed for collisional energy transfer, and the Lennard-Jones potential for estimating collisional frequency. The employed parameters were obtained by fitting MESMER's simulated collision frequency and collisional relaxation rate to the results from Molecular Dynamics calculations, as described in the next section. The values used for the smaller systems (< 39 atoms) were: $\langle \Delta E_{down} \rangle$ = 145 cm^{-1}; ε_{LJ} = 200 K; σ_{LJ} = 10 Å. For the larger systems the values $\langle \Delta E_{down} \rangle$ = 185 cm^{-1}; ε_{LJ} = 550 K; σ_{LJ} = 11 Å were used. N_2 was assigned as bath gas, with Lennard-Jones parameter values ε_{LJ} = 91.85 K and σ_{LJ} = 3.919 Å. Energy grains were set to span values up to 20 k_BT above the highest stationary point and their size was set to 30 cm^{-1}.

S2 Estimation of thermalization rates with Molecular Dynamics.

S2.1 Introduction

During many atmospheric reactions of interest, the product state has a lower total energy than the reactant state. As a result, the initial temperature of the product(s) will be significantly higher than the reactant(s). In the atmosphere, collisions with atmospheric gases (N_2, O_2, etc.) will thermalize the products, bringing the temperature into equilibrium. However, quantifying how this process works is not trivial. Models for the energy transfer processes involved in molecular collisions have certainly been developed (Michael et al., 2002; Miller and Klippenstein, 2006; Pilling and Robertson, 2003; Senosiain et al., 2006), and are included in master equation solving software such as MESMER (Glowacki et al., 2012) used to describe complex gas-phase reaction kinetics. However, these models may be somewhat limited; in particular, they have been developed for and demonstrated to work on rather small molecules and it is unknown how well they may be applied to describe thermalization in larger gas-phase molecules. In this work, we use classical molecular dynamics simulations with empirical force fields to model the thermalization of some of the studied ROOR' compounds as they undergo collisions in a nitrogen atmosphere. Then, we demonstrate how to use our results to obtain the parameters for the stochastic models for thermalization used in MESMER. It is worth noting that the values for these parameters offered by the

software as a default should be used with caution, as they may lead to significant underestimation of the thermalization rate of larger molecules.

S2.2 Potential Models

We used LAMMPS (Plimpton, 1995) to run classical molecular dynamics simulations. OPLS-AA (Jorgensen et al., 1996; Jorgensen and Tirado-Rives, 2005; Kaminski et al., 2001) served as a baseline forcefield for describing a large atmospheric molecule. We used the LigParGen online server (Dodda et al., 2017) to automatically generate a LAMMPS data file for each molecule. In this work, we focus in particular on some molecules which contain peroxide bonds (ROOR'). Since peroxides are not specifically included in the OPLS-AA parameter set we incorporate Lennard-Jones potential parameters, partial charges, bond, and angular terms derived elsewhere for simulations of peroxide and peroxyl groups (Garrec et al., 2014). To model nitrogen molecules, we use a simple model for diatomics, consisting of two Lennard-Jones atoms linked by a rigid bond. No electrostatic interactions are included. The original source for the model is Cheung and Powles (1975). However, we copied the parameters from a later paper (Lee and Kim, 2014), which mistakenly switched the value of ε between O_2 and N_2. As a result, in the model we adopted we had σ_N = 3.31 Å, ε_N/k_B = 61.6 K, with a bond length of 1.1 Å. We did test simulations using the correct value of ε_N/k_B = 37.3 K and found no significant difference in the results. Since the energetics of dilute gases are dominated by kinetic energy, it is not surprising that small differences in the potential model would not have a noticeable effect on our findings. It is also worth noting that both the OPLS-AA parameters, and the nitrogen parameters, were derived for simulations of molecules in aqueous environments and liquid nitrogen, respectively, and so it is worth considering whether they can be applied to a gas phase simulation. Recent work has shown that simulations of protein ions in the gas phase are more or less accurate using parameter sets designed for solvated biomolecules, and rather large reductions in the partial charges are needed to cause appreciable effects (Lee et al., 2019). As far as the nitrogen model is concerned, it has been used previously for simulations of gas phase nitrogen and has been shown to perform well (Lee and Kim, 2014; Wang et al., 2020).

S2.3 Simulation methodology

Our initial simulation box consisted of one analyte molecule in the center of the box, surrounded by randomly placed nitrogen molecules. The cubic box length L = 400 Å, and 1540 N_2 molecules were added to give a pressure P = 1 atm. Other simulations were done with 385 gas molecules, P = 0.25 atm. We consistently used a timestep of 0.5 fs throughout the work. The SHAKE algorithm was used to hold the N_2 bond length constant, as well as any OH bonds in the analyte molecules. Systems were equilibrated in the NVT ensemble for 5 ns using two different Nose-Hoover thermostats to separately maintain the temperature of the analyte molecule and the N_2 gas. The initial temperature of the analyte T_{molec} was set to 800 K, with the nitrogen temperature T_{gas} set to 300 K. After equilibration, the thermostats were removed and the remainder of the simulation proceeded using NVE integration. As the simulation proceeded collisions between gas and analyte served to bring the temperature of the gas and the analyte closer together. Simulations were run long enough so that the overall temperature became uniform, typically 25 to 50 ns.

S2.4 Results and discussion

In Figure S3 we plot $\Delta T(t) = T_{molec} - T_{gas}$ as a function of the simulation time. There is considerable variation in individual simulation runs, so we average over several simulations to reduce the statistical noise.

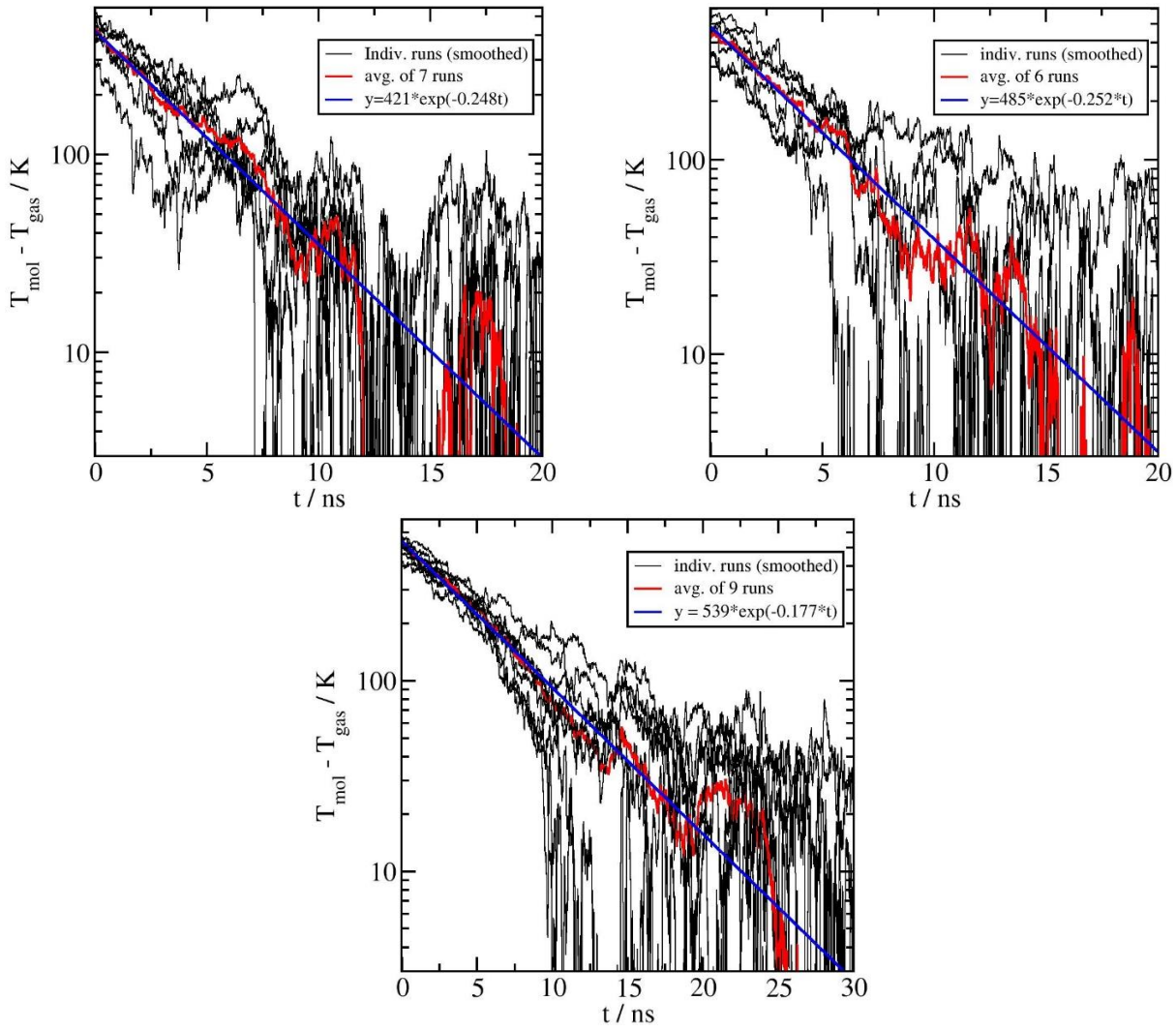

Figure S3: Temperature difference between analyte molecule and surrounding gas for $(EtOOEt)H^+$ (top left), and isomer M3 of the decomposition mechanism of EtOOEt (top right) and ROOR derived from OH oxidation of cyclohexene (bottom). Individual simulation runs are shown in thin black lines, with the average over all simulations in red. The blue line is a fit to an exponential function $\Delta T(t) = Ae^{-Bt}$, with the numerical values of the fit parameters given in the legend.

We find that a single exponential function of the form:

$$\Delta T(t) = Ae^{-Bt} \quad \text{(S1)}$$

fits the temperature difference well in all cases we have studied. The inverse of the constant B in Equation S1 can be interpreted as a characteristic time. For the systems we have studied, and with a gas pressure of 1 atm, this time is on the order of 1 to 10 ns; however, there is considerable variation for different molecules. In the examples we focus on here, we note that the cyclohexene derived ROOR' take s longer to reach the same temperature as the gas compared to the two ethyl peroxide dimers (ca. 5.5 ns vs. 4 ns). By post-processing the trajectories, we obtained more information about the collision events. We define a collision starting if either a nitrogen atom gets closer than 4 Å to one of the atoms in the analyte molecule, and ending when both nitrogen atoms are further away than

4 Å from all of the atoms in the analyte. One complication is the possibility of multiple gas molecules colliding simultaneously; to mitigate against this rare occurrence we ran more simulations with a reduced gas pressure of 0.25 atm. This analysis allows us to compute the gas collision frequency f_{coll}.

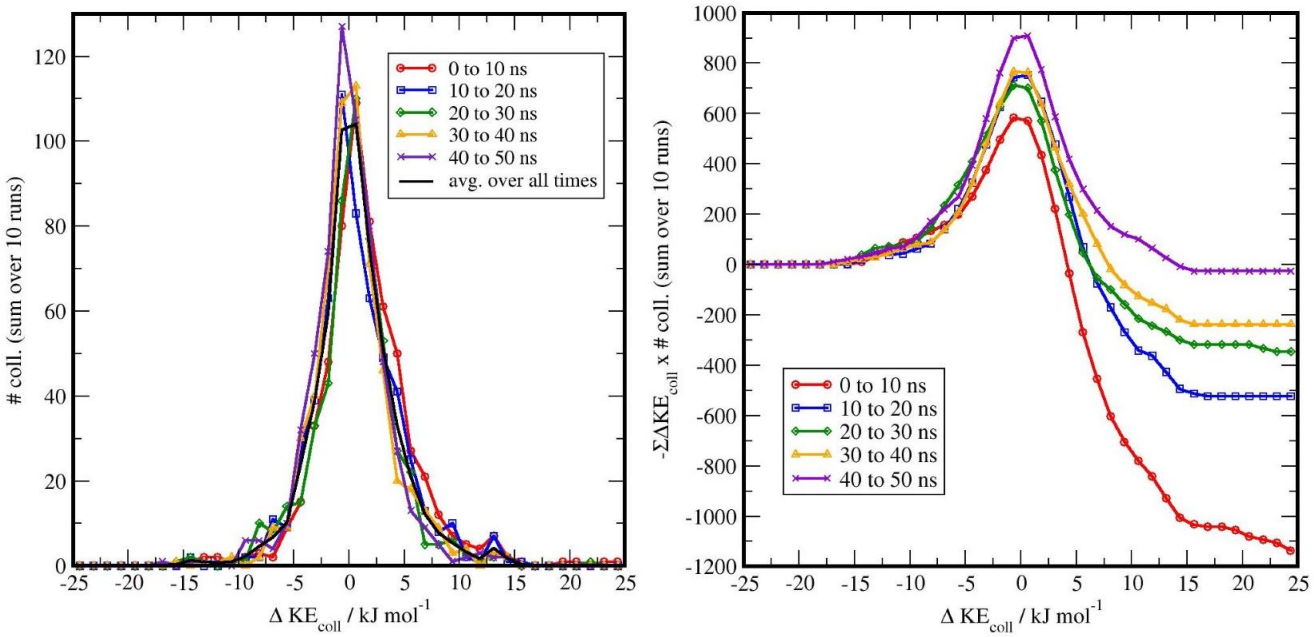

Figure S4: Left: Histogram of the change in the kinetic energy of the colliding gas molecule ΔKE_{coll} during 10 independent simulations with the (EtOOEt)H$^+$ molecule. Right: Cumulative sum of the change in kinetic energy of N_2 before/after each collision ($\sum \Delta KE_{coll}$), multiplied by the number of collisions of that energy. The quantity is multiplied by -1 so that the sum over all collision energies represents the total energy lost by the analyte molecule during each time interval, over the course of 10 individual simulations. The density of N_2 is 0.25 atm.

Table S1: Summary table. $1/B$ is the characteristic time decay constant in Equation 1 from the average of several simulations with 1 atm gas pressure. f_{coll} and $\langle KE_{coll} \rangle$ are the average gas collision rate and kinetic energy transfer from several simulations with 0.25 atm, respectively.

Analyte	$1/B$ (ns)	f_{coll} (ns^{-1})	$\langle KE_{coll} \rangle$ $(kcal.mol^{-1})$
M1 (EtOOEt)	4.0	5.98	0.715
M3 (EtOOEt)	4.0	6.19	0.519
M3 (Cyclohexene + OH)	5.6	7.85	0.996

Another quantity of interest is the energy transfer per collision. We compute the kinetic energy of the gas molecule as an average, using velocities spanning from 3.0 ps to 2.5 ps before/after each collision event. Then we can compute the change in kinetic energy $\Delta KE_{coll} = KE_{after} - KE_{before}$. There is a large variation in the ΔKE_{coll} measured in each collision. In Figure S4 we show a histogram of the ΔKE_{coll} for all collisions during a series of 10 simulation runs. We see that the probability of collisions which lower the KE of the colliding gas molecule is nearly the same as those which raise the KE. The overall temperature equilibration must therefore arise from the relatively small asymmetry in this histogram, which we see from Figure S4 becomes more symmetric as the simulation proceeds and the temperatures of the gas and analyte become closer (Tardy and Rabinovitch, 1977). In Table S1 we summarize the values of the temperature decay time constant 1/B, the gas collision frequency f_{coll} and the average

kinetic energy change per collision $\langle KE_{coll} \rangle$ for three different molecules of interest. These quantities will be used in comparison with the MESMER stochastic models to improve the calculations of reaction rates in MESMER.

S2.5 Fitting MESMER parameters

Table S2: Selected Lennard-Jones parameters and resulting collision frequency f_{coll} and fitted ΔE_{down} value for MESMER simulations at 1 atm.

Species	ε/k_B (K)	σ (Å)	f_{coll} (ns^{-1})	ΔE_{down} $(kcal.mol^{-1})$
M1 (EtOOEt)	200	10	23.2	0.415
M3 (Cyclohexene + OH)	550	11	30.0	0.529

A series of MESMER simulations were done with $EtOOEtH^+$ and the isomer M3 of the ROOR derived from cyclohexene + OH oxidation, varying Lennard-Jones parameters ε and σ in order to find the combination that yields a value of f_{coll} at 1 atm that agrees with results from MD calculations. For the smaller molecule, these values were ε/k_B = 200 K and σ = 10 Å, while for the larger species the selected values were ε/k_B = 550 K and σ = 11 Å (Table S2). The resulting f_{coll} values at 1 atm were 23.2 ns^{-1} and 30.0 ns^{-1} for M1 (EtOOEt) and M3 (Cyclohexene + OH) respectively, being very close to the MD values, assuming that the collision frequency is linearly dependent to pressure. The selected parameter values for M1 (EtOOEt) deviate significantly from values empirically fitted for thermalization of hexane (ε/k_B = 343 K and σ = 6.25 Å) (Hippler et al., 1983), a similarly sized molecule, and may represent an unrealistic description of the Lennard-Jones potential well. However, the obtained values were selected to yield a f_{coll} that agrees with the MD results, and do not interfere with any other function in MESMER's model. Having fixed those parameters, another series of MESMER simulations were done where the investigated species starts at a temperature of 800 K, varying the exponential-down model parameter $\langle \Delta E_{down} \rangle$. The obtained time-dependent internal energy profiles were then compared to the results from MD calculations. The $\langle \Delta E_{down} \rangle$ value yielding the thermalization curve with closest agreement with results from MD calculations, shown in Table S2 and Figure S5, was selected for use in this study.

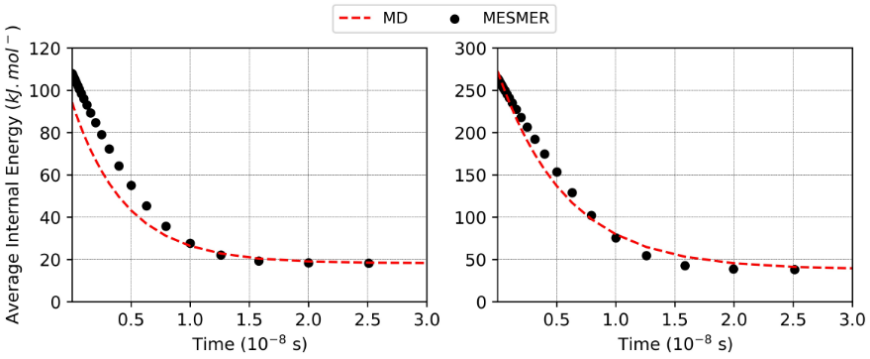

Figure S5. Collisional relaxation curves obtained from MD and MESMER calculations for $EtOOHEt^+$ (a) and isomer M3 of the cyclohexene + OH oxidation derived ROOR (b), at 298.15 K and 1 atm. In both methods the starting temperature of the analyte is 800 K. Fitted Lennard-Jones parameters and exponential-down values are: a) $\langle \Delta E_{down} \rangle$ = 145 cm^{-1}; ε_{LJ} = 200 K; σ_{LJ} = 10 Å; b) $\langle \Delta E_{down} \rangle$ = 185 cm^{-1}; ε_{LJ} = 550 K; σ_{LJ} = 11 Å.

S3 Reaction Mechanism and Energetics.

The general mechanism for fragmentation of ROOR' and ROOH are shown in Scheme 2 and 3 respectively. The calculated Potential Energy Surfaces are depicted in Figures S6-13. Important values for structure and reactivity analysis, such as protonation energies, initial step barrier heights and direct dissociation energies, are shown in Table S3.

S3.1 Model ROOR.

The calculations revealed that the rate-determining step, i.e. the step with the highest barrier on the most favourable reaction pathway, is **R1a** for the MeOOMe system and **R1c** for HOEtOOMe and O=EtOOMe. For the EtOOEt and iPrOOiPr systems, these two steps share a very similar reaction barrier height, and both should be rate-determining. **R1a** involves the cleavage of the peroxy O-O bond with a concerted H migration to the unprotonated peroxy O from its adjacent carbon (1,2 shift), leading to the formation of a proton-bridged alcohol-aldehyde/ketone (**M2**). In step **R1c**, the O-O bond cleavage occurs alongside the 1,2 shift of an organic substituent instead. In most cases, the two fragments formed, an alcohol and a carboxonium ion, rapidly undergo addition to form a protonated acetal/ketal (**M6**). IRC calculations indicate that with O=EtOOMe, this addition does not occur, and **R1c** yields a product complex. Nevertheless, the constituting fragments of the product from **R1c**, either covalently bound or complexed, may suffer barrierless dissociation into **P6**. A third initial step (**R1b**) was found, where the peroxy O-O bond cleavage occurs with concerted H_2 elimination from the C(OO)C carbon atoms, via a ring-like transition state. This channel leads to the formation of a proton-bridged pair of aldehydes/ketones (**P4**), but it was not found to be competitive. The key branching point in the reaction mechanism following **R1a** appears to be the not-so-loosely bound species **M2**. Reaction channels available for **M2** include: nucleophilic attack on the carbonyl C by the alcohol O (**R2a**), producing a protonated hemiacetal/hemiketal (**M3**); H_2 elimination (**R2b**), producing the proton-bridged pair of aldehydes/ketones (**P4**); barrierless dissociation (**R2c** or **R2d**) into alcohol + protonated aldehyde/ketone (**P1**) or protonated alcohol + aldehyde/ketone (**P2**). Species **M3** may further react by a 1,3-H transfer to the hydroxyl O, concerted with a C-OH bond cleavage (**R3a**), yielding a H_2O:carboxonium ion complex (**M4**). Complex **M4** fragments may in turn fly apart into **P3** + H_2O (**R4b**), or react with each other producing **P2** (**R4a**). The proton-bridged pair of aldehydes/ketones (**P4**) can also dissociate (**R5**) into its constituting fragments (**P5**). Three channels involving direct dissociation of the initial reactant without rearrangement are available, but none was observed to be competitive for the model ROOR' systems: Heterolytic C-O bond cleavage yielding a hydroperoxide R'OOH and the corresponding carbocation R^+ (**R9**); Homolytic O-O bond cleavage yielding an alkoxy radical R'O$^\bullet$ and an alcohol radical cation $ROH^{\bullet+}$ (**R10**); and a homolytic analogue of **R9**, yielding a hydroperoxide radical cation $R'OOH^{\bullet+}$ and a carbon centered radical R$^\bullet$ (**R11**).

Table S3. Protonation energy, initial step barrier heights and direct dissociation energies calculated at the RHF-RCCSD(T)-F12a/VDZ-F12 // ωB97XD/aug-cc-pVTZ level of theory for ROOR and ROOH decomposition. All values correspond to zero-point corrected energies, given in kcal mol^{-1}, relative to the lowest energy protonation isomer of the initial charged species. Species structures are given in Scheme 2 and 3.

(ROOR')H$^+$	**ROOR' + H_3O^+ – H_2O**	**TS 1a**	**TS 1b**	**TS 1c**	**TS 1d**	**P9**	**P10**
Me-OO**H**-Me$^+$	15.38	21.06	23.35	---	---	72.26	49.97
Et-OO**H**-Et$^+$	23.40	15.43	20.28	15.35	---	43.44	46.07
iPr-OO**H**-iPr$^+$	28.54	12.25	22.41	12.26	---	35.03	45.94
HOEt-OO**H**-Me$^+$	32.88	29.54	---	22.00	---	43.83	68.15
HO=Et-OO-Me$^+$	27.03	36.52	---	21.34	---	61.16	38.84
(Cyclohexene + OH)	52.63	28.26	---	26.35	---	37.18	33.56
(Cyclohexene + O_3)	56.03	35.34	---	26.31	20.40	30.00	34.83
(ROOH)H$^+$							

Me-OO**H**-H^+	4.29	10.95	---	---	---	---	---
Me-**H**OO-H^+	8.32	---	---	---	---	64.75	47.82
Et-OO**H**-H^+	7.58	4.52	---	3.08	---	---	---
Et-**H**OO-H^+	14.15	---	---	---	---	33.97	42.01
iPr-OO**H**-H^+	10.97	2.07	---	1.21	---	---	---
iPr-**H**OO-H^+	18.97	---	---	---	---	24.53	39.28
tBut-OO**H**-H^+	13.62	---	---	0.12	---	---	---
tBut-**H**OO-H^+	23.34	---	---	---	---	16.61	37.43
H_2OEt-OO-H^+	27.04	25.18	---	22.25	---	37.52	40.02
HO=Et-OO-H^+	21.31	32.47	---	25.79	---	81.63	38.68
(Cyclohexene + OH)	36.56	22.24	---	16.23	---	19.02	24.04
(Cyclohexene + O_3)	42.99	31.86	---	22.47	25.14	22.76	32.76

Considering the alky-substituted ROOR' systems, faster fragmentation rates were observed with increasing degree of substitution (R = Me < R = Et < R = iPr). The reason behind this trend is an increasing exothermicity of protonation by H_3O^+ and decreasing barrier heights for rate-determining steps **R1a** and **R1c**. The first of these factors may be explained by the greater electronic density introduced into the peroxy oxygens by methyl groups via inductive effects, increasing the proton affinity of the peroxide. The second factor can be understood by examining the part of the molecule where a 1,2-migration occurs during steps **R1a** and **R1c** when, en route to the transition state, the α-carbon atom increasingly becomes electron-deficient and assumes a sp^2 character. The C-H σ-bonds present in an adjacent methyl group may interact with this C atom's partially empty p-orbital, stabilizing the transition state by hyperconjugation. Thus, in comparison to the MeOOMe system, the presence of one methyl group (EtOOEt) lowers the **R1a** reaction barrier by 5.7 kcal mol^{-1}; and a second methyl group (iPrOOiPr) lowers this barrier by an additional 3.1 kcal mol^{-1}. In reaction step **R1c**, the group undergoing 1,2-shift to the oxygen atom is one of these methyl groups, which cannot participate in hyperconjugative stabilization of the transition state. Yet within the same reacting system, steps **R1a** and **R1c** have very similar barrier heights. Additional insight into the energetics of these competing channels is brought by analysing the kinetics of Baeyer-Villiger reactions (Clayden et al., 2012). During the rearrangement, a part of the positive charge may be allocated on the group being transferred, and therefore groups that better accommodate this charge stabilize the transition state to a greater degree. The importance of such factor is evidenced by the dissociative character of the rearrangement in the transition states of **R1a** and **R1c**, where the shifting group sits closer to the C than to the O atom. Methyl cation is a better leaving group than H^+, and therefore as far as the migrating group is concerned, a 1,2-shift involving the former (**R1c**) is more favourable than with the latter **(R1a**).

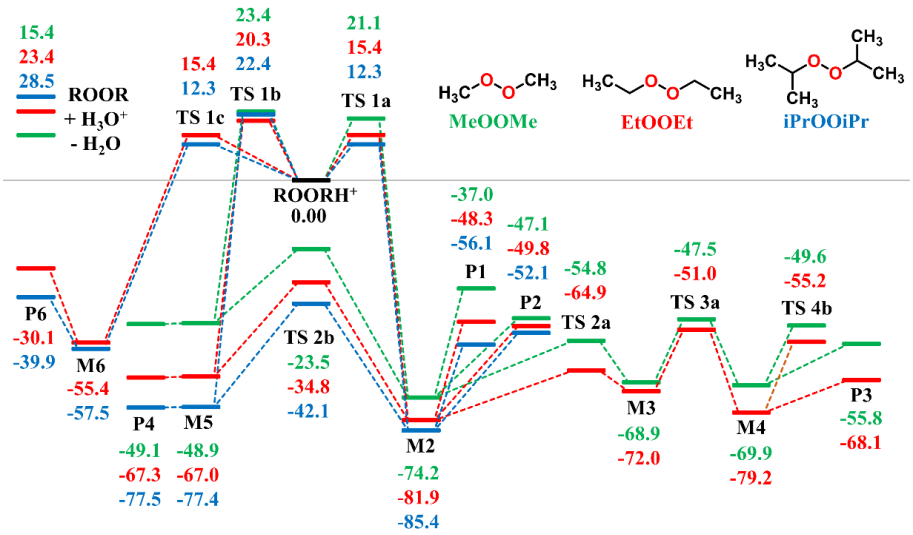

Figure S6. Potential energy surface calculated at the RHF-RCCSD(T)-F12a/VDZ-F12// ωB97XD/aug-cc-pVTZ level of theory, for decomposition of Me-OO-Me (green), Et-OO-Et (red) and iPr-OO-iPr (blue) following protonation in the gas phase. Molecular structures for stationary points are shown in Scheme 2. Values given are relative zero-point corrected energies in kcal mol^{-1}.

At the lower limit of excess energy, significant decomposition of MeOOMe occurs only after ~1 s, the major products being protonated methanol + formaldehyde (**P2**) and protonated formaldehyde + methanol (**P1**) with a branching ratio of 0.92 and 0.08 respectively. End products and respective branching ratios for decomposition of EtOOEt are **P6** (0.62), **P2** (0.31), **P1** (0.06) and **P3** (0.01); while those for iPrOOiPr are **P6** (0.55), **P2** (0.32) and **P1** (0.13). Species **M3** is not a stable minimum in the PES of iPrOOiPr, since geometry optimizations lead to a different structure. This result makes sense considering the high steric strain present in such a molecule. A transition state for **R2a** was also not found for iPrOOiPr, so this step and all those that would follow it are assumed to be unavailable for this ROOR. Observing the PES for the channels available for intermediate **M2**, shown in Figure S6, it would be expected that most of MeOOMe and EtOOEt reacting through **R1a** would subsequently follow **R4a**, the most energetically favourable dissociation route. However, reaction dynamics simulations revealed that **P3** is only a minor fragmentation product. The reason behind this result may be that, upon reaching **M2**, the reacting system accumulates considerable excess internal energy, enough to promote immediate dissociation into **P1** or **P2** before a significant fraction of species can further react to yield **M4** (Schalley et al., 1997).

As for the systems containing oxygenated substituents, HOEtOOMe and O=EtOOMe, relatively less fragmentation was observed within relevant time scales. At 1.023 mbar, ~68.2% of HOEtOOMe and ~24.6% of O=EtOOMe are left intact after 100 μs, the major fragmentation product being **P6** in both cases. As described in the beginning of this section, interconversion between the initial protonation isomers was found to be fast. Very low-lying transition states were found for steps **R0b** in the PES of HOEtOOMe, whereas no transition states were found for the O=EtOOMe counterparts. Thus, for the sake of analysis of the rate of decomposition of these two peroxides, all of their initial reaction step transition states can be assumed to be connected to their most stable protonation isomer, HOEtOO**H**Me$^+$ and **H**O=EtOOMe$^+$, shown in Figure S7. Both species have an intramolecular H-bond between a peroxy group's and the substituent's oxygen atom, in a six-member ring-like conformation. This factor grants extra stability to these protonation isomers, as seen by the larger exothermicity of reaction of the parent peroxides with H_3O^+, compared to EtOOEt (Table S3). Calculations with O=EtOO**H**Me$^+$ indicate that the most favourable conformation of this species is not a minimum in the PES, since the proton is transferred to the carbonyl-oxygen during geometry optimisation. By having the carbonyl as the protonation site, reactant

HO=EtOOMe$^+$ is further stabilized by resonance. Higher energy protonation isomers HOEt**H**OOMe$^+$ and O=Et**H**OOMe$^+$ also make an intramolecular H-bond, but in a more rigid five-member ring-like conformation, which is weaker due to the less then optimal O---H-O angles. No such H-bond is present in the **R1c** and the two **R1a** transition states available in the PES of HOEtOOMe (Figure S7), which partly explains the higher barriers, and therefore the lower reaction rates. The same is true for the **R1c** and the lowest energy **R1a** transition state in the PES of O=EtOOMe. IRC calculation with the **TS1a** connected to isomer HOEtOO**H**Me$^+$ revealed that this reaction step would produce the protonated hemiacetal (**M3**) instead of **M2**, even though the latter is lower in energy.

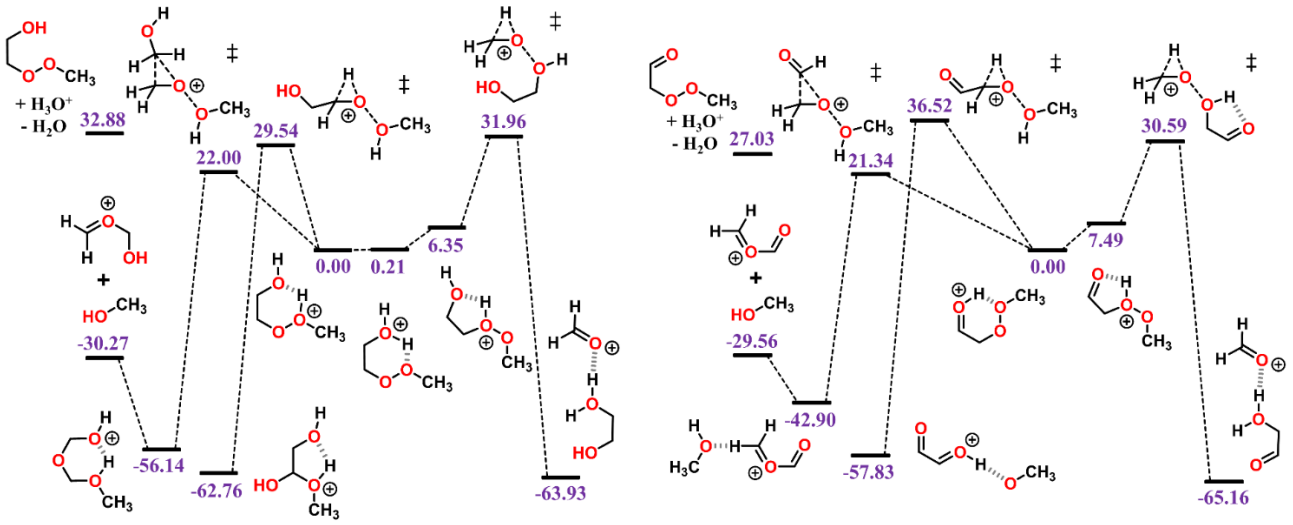

Figure S7. Potential energy surface calculated at the RHF-RCCSD(T)-F12a/VDZ-F12//ωB97XD/aug-cc-pVTZ level of theory for the initial steps in the decomposition of HOCH2CH2OOMe (left) and OCHCH2OOMe (right) following protonation in the gas phase. Values given in purple are relative zero-point corrected energies in kcal mol^{-1}.

The absence of H-bonds in transition states described above results from a stereochemical constraint of such reactions (Clayden et al., 2012), where the migrating group has to be anti-periplanar to the leaving (alcohol) group. During the rearrangement, the electrons in the breaking C-C (or C-H) σ orbital gradually move into the empty O-O σ* orbital. Optimal overlap between these orbitals is achieved with an anti-periplanar conformation between the two involved moieties. Different to alkyl-substituted systems, HOEtOOMe and O=EtOOMe react only through the channel starting with **R1c**, as a result of the much lower reaction barrier of this step relative to **R1a** (Table S3). Due to resonance, both -CH_2OH and -CHO can accommodate a partial positive charge better than a methyl group, thus stabilizing the **R1c** transition state to a greater degree when taking part in the 1,2-shift. However, -CH_2OH is not as effective in stabilizing an adjacent carbocationic center, having C-H bonds available for hyperconjugation, but also an electron-withdrawing OH group. As a result, the **R1a** transition encountered by HOEtOO**H**Me$^+$ is not stabilized to the same extent as **R1c**. The -CHO group is moderately electron-withdrawing by induction, producing instead a destabilizing effect on the **R1a** transition state encountered by **H**O=EtOOMe$^+$, yielding the largest barrier for this step (36.5 kcal mol^{-1}) among the studied model ROOR' systems.

The reaction of protonated AcOOAc, which follows a different mechanism, is shown through its PES in Figure S8. Initial reaction with H_3O^+ can occur with protonation of a carbonyl-oxygen or a peroxyl-oxygen. Since a protonated carbonyl favors a planar geometry, the former may produce two isomers (**E** and **Z**), depending on which "side" of the functional group the proton is transferred to. However, the torsional barrier between the two isomers is relatively low (~11 kcal mol^{-1}) and interconversion occurs at time scales shorter than other reaction pathways. The peroxyl-oxygen protonated AcOOAc was not found to be a stable minimum, since geometry

optimization leads instead to a dissociation product complex, where the fragments are an acylium ion (Ac^+) and peracetic acid (AcOOH). This result is similar to what was obtained for calculations with protonated acetic acid by Shi et al. (2015), where protonation at the hydroxyl-oxygen leads to a H_2O : acylium ion complex. The charged AcOOH:Ac^+ complex is however strongly bound, and reassociation with concerted H transfer to the carbonyl-oxygen has a very low barrier (1.37 kcal mol^{-1}), producing the more stable Z-isomer of the carbonyl-protonated AcOOAc. The only reaction pathway left to consider is a rearrangement available for the **E** and **Z** isomers, leading to a protonated acetic methylcarbonic anhydride ($AMCAH^+$). The barrier for this reaction is low compared to the energy released during protonation and the produced anhydride is stable. Reaction dynamics simulations revealed that after 100 μs, at 1.023 mbar and 298.15 K, about 18% of protonated AcOOAc is converted to $AMCAH^+$ and only ~1% yields the fragmentation products (AcOOH + Ac^+).

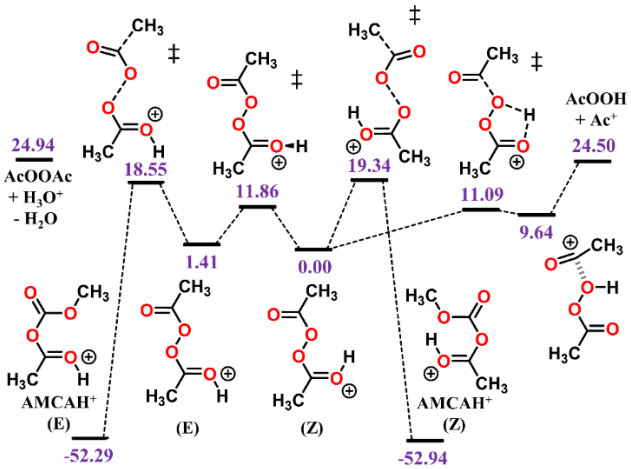

Figure S8. Potential energy surface calculated at the RHF-RCCSD(T)-F12a/VDZ-F12// ωB97XD/aug-cc-pVTZ level of theory for the reaction of AcOOAc following protonation in the gas phase. Values given in purple are relative zero-point corrected energies in kcal mol^{-1}.

S3.2 Model ROOH.

For ROO**H**$_2^+$ the initial step with the lowest barrier is of the **R1a** type for R=Me and **R1c** type for R=Et, iPr or tBut, analogous to the ones found for ROOR, but in this case the molecule dissociates into a proton-bridged aldehyde/ketone : water complex (**M2**) or a carboxonium ion : water complex (**M6**). The trend in energetics for protonation exothermicity and initial step barrier height is the same as for the ROOR analogues, where the former increases and the latter decreases with larger substituents (R = Me < R = Et < R = iPr), likely due to the same factors discussed in the ROOR section. However, the energy released during protonation by H_3O^+ is considerably smaller for ROOH systems, which could reduce the proportion of molecules that react at non-thermal rates. On the other hand, the barrier heights for the (rate limiting) step **R1a** are also much lower for the alkyl-substituted ROOH systems, meaning thermal reaction rates are faster. Given that any of the considered R groups have a greater electron-donating effect than a hydrogen, a ROOH system has a smaller proton affinity and its O-O bond is more polarized compared to a ROOR.

Reaction dynamics simulations for MeOO**H**$_2^+$ revealed that this species decomposes only at thermal rates across the pressure range considered here, which is evidenced by the single, pressure dependent decay curve (Figure 5). At 1.023 mbar, about ~17% of MeOO**H**$_2^+$ is decomposed after 100 μs, opposed to ~0% observed for MeOO**H**Me$^+$ in the same conditions. EtOO**H**$_2^+$, iPrOO**H**$_2^+$ and tButOO**H**$_2^+$ show very low barriers for step **R1c** (3.08, 1.21 and 0.12 kcal mol^{-1} respectively), and all three species are entirely (>99%) fragmented within ~1 μs. The final products of MeOO**H**$_2^+$ decomposition are protonated formaldehyde + H_2O (**P1**, 9.3%) and formaldehyde + H_3O^+ (**P2**, 7.7%).

Water addition to the protonated carbonyl in **M2** is also possible for the MeOOH system, but it was not found to be an important reaction channel since the product is higher in energy and subsequent H_2 elimination (**R3b**) has a very high barrier. The major fragmentation products of all other alkyl-substituted ROO**H**$_2^+$ are a carboxonium ion + H_2O (**P3**). Complex **M6**'s constituting fragments can react with each other via nucleophilic substitution producing a protonated alcohol : aldehyde/ketone complex (**M7**), which can also undergo barrierless dissociation, yielding **P7**. However, this route was not observed to be competitive.

In contrast, protonation isomer RO**H**OH$^+$ is rather inert. Apart from isomerization into ROO**H**$_2^+$, only the three direct dissociation channels are available these: Heterolytic C-O bond cleavage yielding H_2O_2 and the corresponding carbocation R^+ (**R8**); Homolytic O-O bond cleavage yielding OH radical and a ROH$^{\bullet+}$ radical cation (**R9**); and a homolytic analogue of **R8**, yielding $H_2O_2^{\bullet+}$ radical cation and a carbon centered radical R$^\bullet$ (**R10**). Each of these channels was investigated for the other ROOH systems but, except for **R8** with tButO**H**OH$^+$, none were observed to contribute to decomposition within significant timescales, under the lower limit of excess energy scenario. For MeO**H**OH$^+$, the most favorable of these channels is **R9**, but the required energy is so high that the system would rather react through **R0a** to give MeOO**H**$_2^+$. **R8** dissociation energy decreases fast with increasing alkyl-substituent size, as the electron donating methyl groups stabilize the formed carbocation, and this step becomes the most favorable for the other RO**H**OH$^+$ systems. At 1.023 mbar, about 89.8% of tButO**H**OH$^+$ fragments into tert-butyl cation + H_2O_2 within 100 µs, while other RO**H**OH$^+$ remain unreacted.

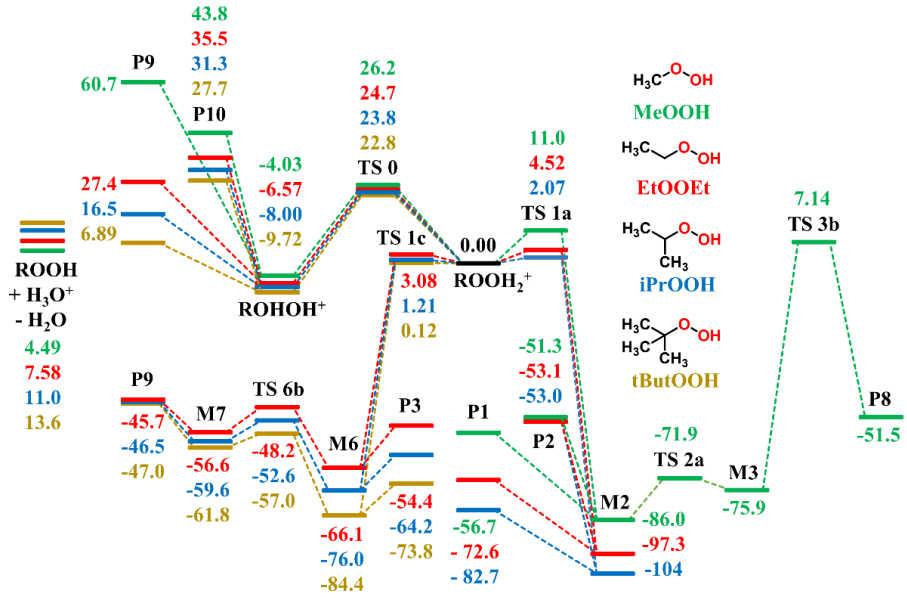

Figure S9. Potential energy surface calculated at the RHF-RCCSD(T)-F12a/VDZ-F12// ωB97XD/aug-cc-pVTZ level of theory, for decomposition of MeOOH (green), EtOOH (red), iPrOOH (blue) and tButOOH (yellow) following protonation in the gas phase. Molecular structures for stationary points are shown in Scheme 3. Values given are relative zero-point corrected energies in kcal mol^{-1}.

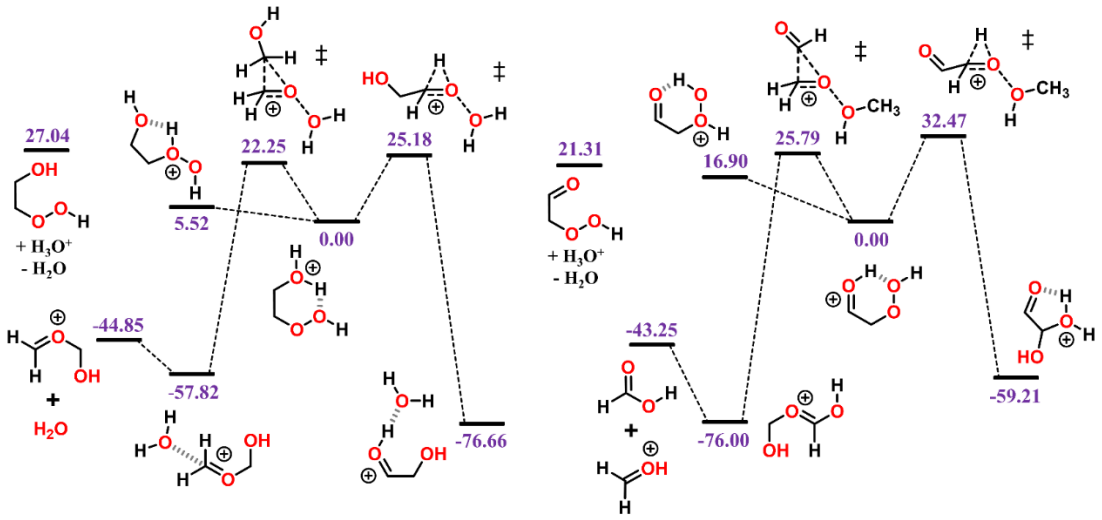

Figure S10. Potential energy surface calculated at the RHF-RCCSD(T)-F12a/VDZ-F12//ωB97XD/aug-cc-pVTZ level of theory for the initial steps in the decomposition of HOEtOOH (left) and O=EtOOH (right) following protonation in the gas phase. Values given in purple are relative zero-point corrected energies in kcal mol^{-1}.

The calculations revealed that following protonation, HOEtOOH and O=EtOOH undergo little to no fragmentation within relevant time scales. Like with HOEtOOMe and O=EtOOMe, initial step **R1c** is favored over **R1a**. After 100 µs at 1.023 mbar, about 14.6% of HOEtOOH has fragmented into **P3**, while no significant amount of O=EtOOH has reacted. The underlying reason for the lower reactivities of these ROOH is the same as described previously for their ROOR' analogues: The intramolecular H-bond which stabilizes the protonated reactant is absent in the transition state of the initial steps **R1c** and **R1a**, resulting in higher reaction barriers (Figure S10). Furthermore, geometry optimizations indicate that the lowest energy conformation of the ROO**H**$_2^+$ isomer of these systems is not stable, undergoing barrierless H transfer to the alcohol/carbonyl group's oxygen, producing the more stable **H**$_2$OEtOOH$^+$ and **H**O=EtOOH$^+$ isomers. The RO**H**OH$^+$ isomers are possible but C-O or O-O scissions (**R8-10**) are unfavorable, and H-shift leading to the hydroxyl/carbonyl-protonated isomers (**R0c**) is very fast.

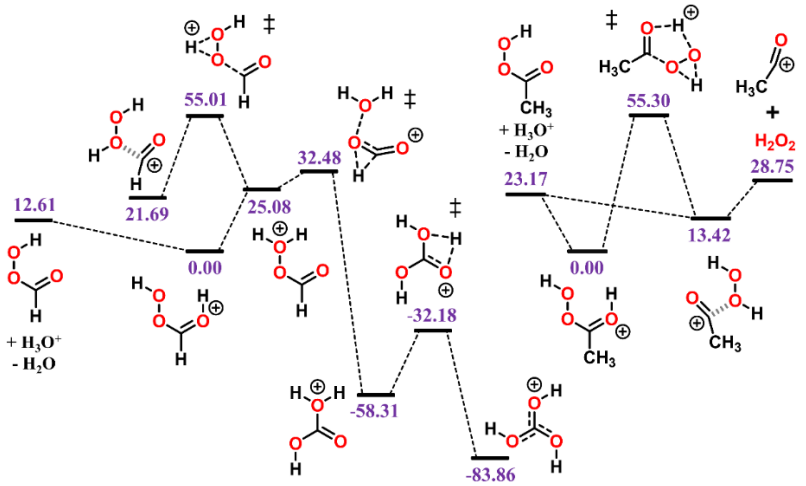

Figure S11. Potential energy surface calculated at the RHF-RCCSD(T)-F12a/VDZ-F12// ωB97XD/aug-cc-pVTZ level of theory for the reaction of peracetic acid (right) and performic acid (left) following protonation in the gas phase. Values given in purple are relative zero-point corrected energies in kcal mol^{-1}.

Decomposition of the protonated peroxy acids follow a different mechanism than that shown in Scheme 3. Their potential energy surface is presented in Figure S11. Two protonation products were found for peracetic acid, the most stable being the carbonyl-oxygen protonated species (**H**AcOOH$^+$). Protonation of the peroxyl-oxygen atom adjacent to the acyl carbon occurs with concomitant C-O(OH) bond scission, leading to formation of an acylium ion (Ac^+) and H_2O_2 complex. The energy required for dissociation of this complex is higher than the excess energy released during protonation, and only ~0.6% of it fragments after 100 μs at 1.023 mbar. Interconversion between the Ac^+:H_2O_2 complex and **H**AcOOH$^+$ is possible but very unfavorable given the high reaction barrier involved (55.3 kcal mol^{-1}). Species AcOO**H**$_2^+$ is not stable, being rapidly converted into **H**AcOOH$^+$. Protonation of any oxygen atom in performic acid may result in a stable product, however the only exothermic channel produces the carbonyl-protonated isomer (**H**OCHOOH$^+$). No transition state was found for proton transfer from the carbonyl to the terminal peroxyl-oxygen, indicating this step should have a very low barrier. The produced isomer OCHOO**H**$_2^+$ has a decomposition reaction channel available that leads to the formation of protonated carbonic acid, however the overall barrier is too high (32.5 kcal mol^{-1}) and it doesn't happen at relevant time scales. Nevertheless, the elemental composition would be retained, and the mass spectrum signal would not be impacted. Similar to peracetic acid, protonation of the oxygen adjacent to the acyl carbon in performic acid would lead to formation of a formyl cation (HCO^+) and H_2O_2 complex.

S3.3 Cyclohexene oxidation products

A new reaction pathway (**R1d**) was found to be available for the ROOR and ROOH derived from ozonolysis of cyclohexene, depicted in Scheme S1. In it, instead of a 1,2-rearrangement of a H or an organyl group like in **R1a** or **R1c**, a more favorable 1,6 H$^+$-transfer occurs alongside the O-O bond scission. This reaction step is possible due to the presence of a carbonyl group situated at a further distance from the peroxide group and, for the ROOR system, it was observed to be dominant among decomposition steps involving rearrangement.

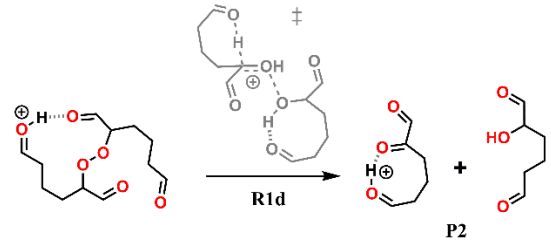

Figure S12. Initial decomposition step R1d, found for ROOR and ROOH derived from cyclohexene ozonolysis.

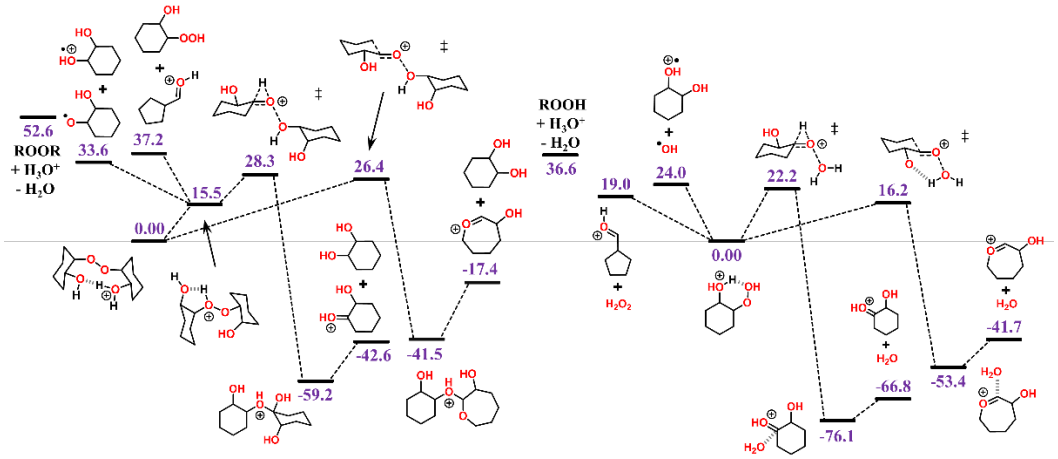

Figure S13. Potential energy surface calculated at the ωB97XD/aug-cc-pVTZ level of theory for reaction following protonation in the gas phase, for the ROOR (left) and ROOH (right) derived from cyclohexene oxidation by OH. Values given in purple are relative zero-point corrected energies in kcal mol^{-1}.

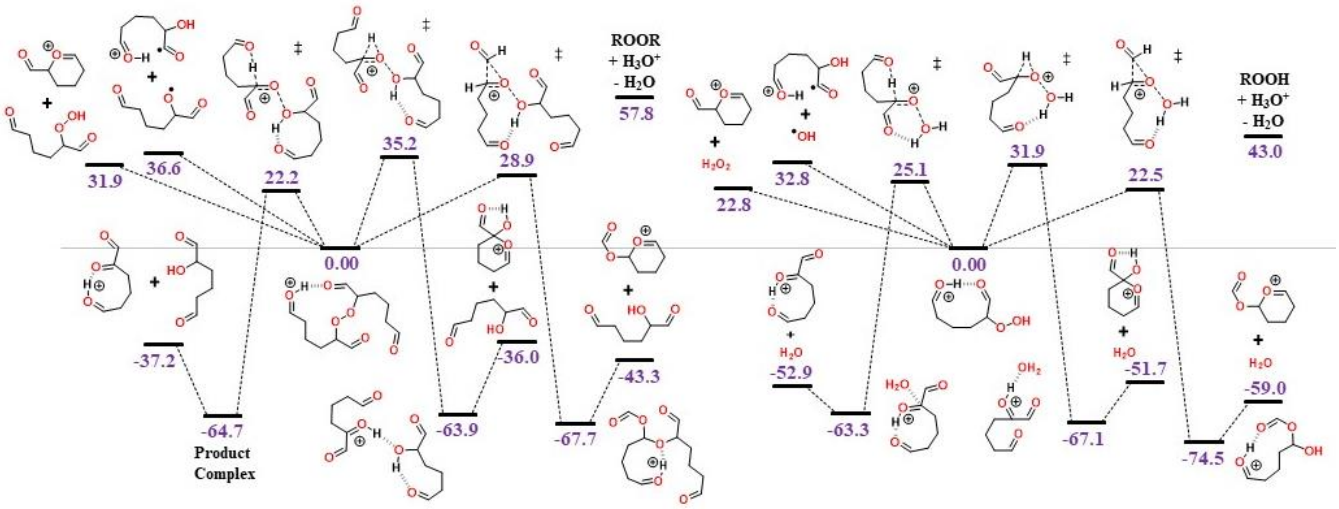

Figure S14. Potential energy surface calculated at the ωB97XD/aug-cc-pVTZ level of theory for reaction following protonation in the gas phase, for the ROOR (left) and ROOH (right) derived from cyclohexene oxidation by O_3. Values given in purple are relative zero-point corrected energies in kcal mol^{-1}.

S3.4 High Energy Collisions.

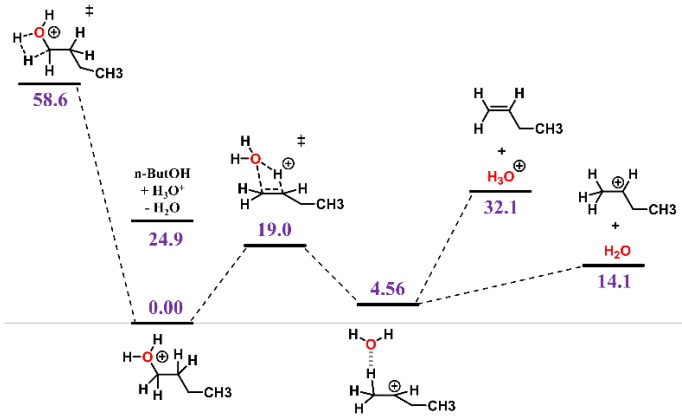

Figure S15. Potential energy surface calculated at the RHF-RCCSD(T)-F12a/VDZ-F12 // ωB97XD/aug-cc-pVTZ level of theory for reaction following protonation in the gas phase, for n-butanol. Values given in purple are relative zero-point corrected energies in kcal mol^{-1}.

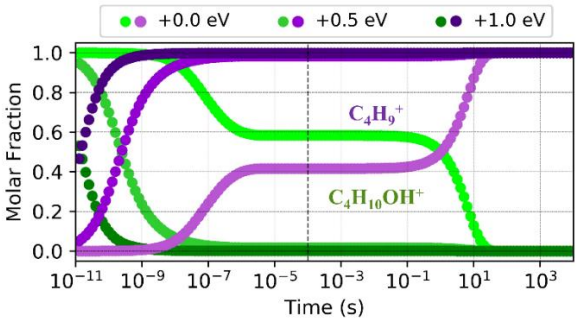

Figure S16. Reaction dynamics simulation results for n-butanol following protonation, under three excess energy scenarios. Graphs represent the time evolution profile of fragmentation, at 298.15 K and 1.013 mbar.

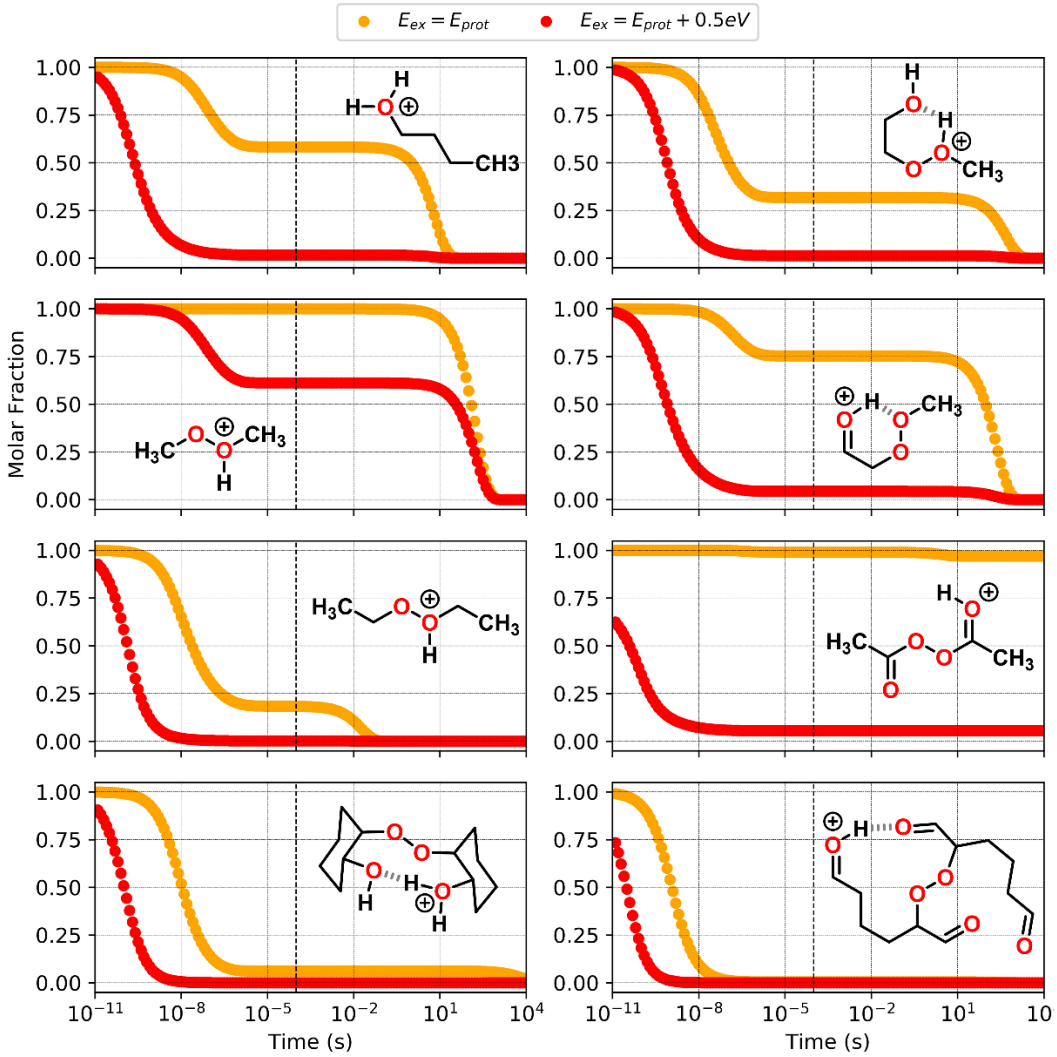

Figure S17. Reaction dynamics simulation results for n-butanol and the investigated ROOR systems, under two excess internal energy scenarios: Protonation energy only (orange) and protonation energy + 0.5 eV (red). Graphs represent the time evolution profile for reaction of initial protonated reactants, at 298.15 K and 1.013 mbar.

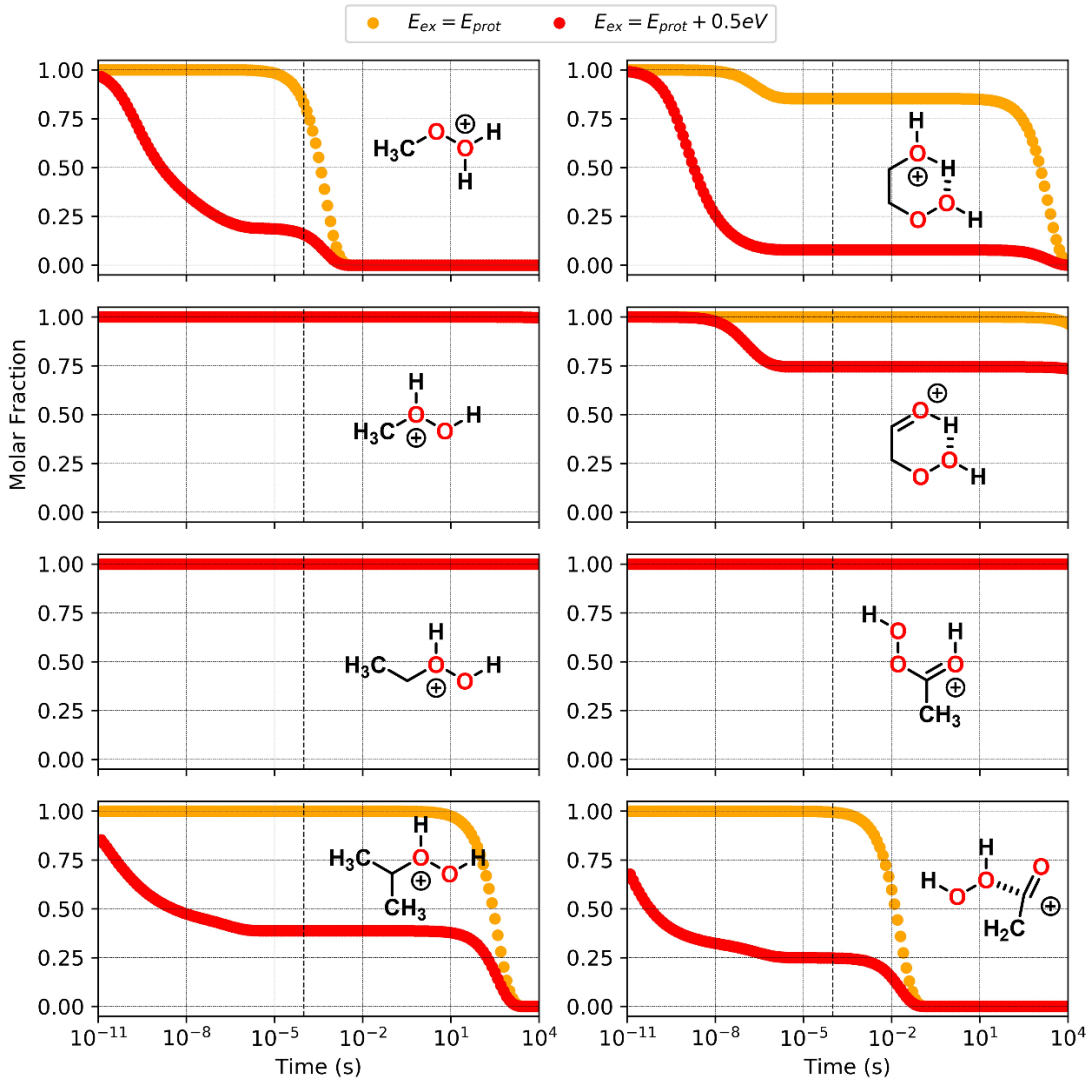

Figure S18. Reaction dynamics simulation results for the investigated ROOR systems, under two excess internal energy scenarios: Protonation energy only (orange) and protonation energy + 0.5 eV (red). Graphs represent the time evolution profile for reaction of initial protonated reactants, at 298.15 K and 1.013 mbar.

References

Cheung, P. S. Y. and Powles, J. G.: The properties of liquid nitrogen, Molecular Physics, 30, 921-949, 10.1080/00268977500102461, 1975.

Clayden, J., Warren, S. G., and Greeves, N.: Organic Chemistry, OUP Oxford, Oxford2012.

Dodda, L. S., Cabeza de Vaca, I., Tirado-Rives, J., and Jorgensen, W. L.: LigParGen web server: an automatic OPLS-AA parameter generator for organic ligands, Nucleic Acids Res, 45, W331-w336, 10.1093/nar/gkx312, 2017.

Eckart, C.: The Penetration of a Potential Barrier by Electrons, Physical Review, 35, 1303-1309, 10.1103/PhysRev.35.1303, 1930.

Garrec, J., Monari, A., Assfeld, X., Mir, L. M., and Tarek, M.: Lipid Peroxidation in Membranes: The Peroxyl Radical Does Not "Float", The Journal of Physical Chemistry Letters, 5, 1653-1658, 10.1021/jz500502q, 2014.

Glowacki, D. R., Liang, C. H., Morley, C., Pilling, M. J., and Robertson, S. H.: MESMER: An Open-Source Master Equation Solver for Multi-Energy Well Reactions, J. Phys. Chem. A, 116, 9545-9560, 10.1021/jp3051033, 2012.

Hippler, H., Troe, J., and Wendelken, H. J.: Collisional deactivation of vibrationally highly excited polyatomic molecules. II. Direct observations for excited toluene, The Journal of Chemical Physics, 78, 6709-6717, 10.1063/1.444670, 1983.

Jorgensen, W. L. and Tirado-Rives, J.: Potential energy functions for atomic-level simulations of water and organic and biomolecular systems, Proceedings of the National Academy of Sciences of the United States of America, 102, 6665, 10.1073/pnas.0408037102, 2005.

Jorgensen, W. L., Maxwell, D. S., and Tirado-Rives, J.: Development and Testing of the OPLS All-Atom Force Field on Conformational Energetics and Properties of Organic Liquids, J. Am. Chem. Soc., 118, 11225-11236, 10.1021/ja9621760, 1996.

Kaminski, G. A., Friesner, R. A., Tirado-Rives, J., and Jorgensen, W. L.: Evaluation and Reparametrization of the OPLS-AA Force Field for Proteins via Comparison with Accurate Quantum Chemical Calculations on Peptides, The Journal of Physical Chemistry B, 105, 6474-6487, 10.1021/jp003919d, 2001.

Lee, M.-T., Orlando, F., Khabiri, M., Roeselová, M., Brown, M. A., and Ammann, M.: The opposing effect of butanol and butyric acid on the abundance of bromide and iodide at the aqueous solution–air interface, Phys. Chem. Chem. Phys., 21, 8418-8427, 10.1039/C8CP07448H, 2019.

Lee, S. and Kim, J.: Molecular Dynamics Simulation Study of Transport Properties of Diatomic Gases, Bulletin of the Korean Chemical Society, 35, 3527-3531, 10.5012/bkcs.2014.35.12.3527, 2014.

Michael, J. V., Su, M. C., Sutherland, J. W., Carroll, J. J., and Wagner, A. F.: Rate Constants For H + O2 + M → HO2 + M in Seven Bath Gases, The Journal of Physical Chemistry A, 106, 5297-5313, 10.1021/jp020229w, 2002.

Miller, J. A. and Klippenstein, S. J.: Master Equation Methods in Gas Phase Chemical Kinetics, The Journal of Physical Chemistry A, 110, 10528-10544, 10.1021/jp062693x, 2006.

Pilling, M. J. and Robertson, S. H.: Master Equation Models for Chemical Reactions of Importance in Combustion, Annual Review of Physical Chemistry, 54, 245-275, 10.1146/annurev.physchem.54.011002.103822, 2003.

Plimpton, S.: Fast Parallel Algorithms for Short-Range Molecular Dynamics, Journal of Computational Physics, 117, 1-19, https://doi.org/10.1006/jcph.1995.1039, 1995.

Schalley, C. A., Dieterle, M., Schroder, D., Schwarz, H., and Uggerud, E.: On the cleavage of the peroxide O-O bond in methyl hydroperoxide and dimethyl peroxide upon protonation, Int. J. Mass Spectrom. Ion Process., 163, 101-119, 10.1016/s0168-1176(97)00001-3, 1997.

Senosiain, J. P., Klippenstein, S. J., and Miller, J. A.: Pathways and Rate Coefficients for the Decomposition of Vinoxy and Acetyl Radicals, The Journal of Physical Chemistry A, 110, 5772-5781, 10.1021/jp054934r, 2006.

Shi, H. C., Wang, Y. L., and Hua, R. M.: Acid-catalyzed carboxylic acid esterification and ester hydrolysis mechanism: acylium ion as a sharing active intermediate via a spontaneous trimolecular reaction based on density functional theory calculation and supported by electrospray ionization-mass spectrometry, Phys. Chem. Chem. Phys., 17, 30279-30291, 10.1039/c5cp02914g, 2015.

Su, T. and Chesnavich, W. J.: Parametrization of the ion-polar molecule collision rate-constant by trajectory calculations, J. Chem. Phys., 76, 5183-5185, 10.1063/1.442828, 1982.

Tardy, D. C. and Rabinovitch, B. S.: Intermolecular vibrational energy transfer in thermal unimolecular systems, Chemical Reviews, 77, 369-408, 10.1021/cr60307a004, 1977.

Wang, L., Ceriotti, M., and Markland, T. E.: Quantum kinetic energy and isotope fractionation in aqueous ionic solutions, Phys. Chem. Chem. Phys., 22, 10490-10499, 10.1039/C9CP06483D, 2020.